https://doi.org/10.1038/s44310-024-00009-6

Deterministic quasi-continuous tuning of phase-change material integrated on a high-volume 300-mm silicon photonics platform

Rui Chen[1,3] ✉, Virat Tara[1,3], Minho Choi[1], Jayita Dutta[1], Justin Sim[1], Julian Ye[2], Zhuoran Fang[1], Jiajiu Zheng[1] & Arka Majumdar[1,2] ✉

Programmable photonic integrated circuits (PICs) consisting of reconfigurable on-chip optical components have been creating new paradigms in various applications, such as integrated spectroscopy, multi-purpose microwave photonics, and optical information processing. Among many reconfiguration mechanisms, non-volatile chalcogenide phase-change materials (PCMs) exhibit a promising approach to the future very-large-scale programmable PICs, thanks to their zero static power and large optical index modulation, leading to extremely low energy consumption and ultra-compact footprints. However, the scalability of the current PCM-based programmable PICs is still limited since they are not directly off-the-shelf in commercial photonic foundries now. Here, we demonstrate a scalable platform harnessing the mature and reliable 300 mm silicon photonic fab, assisted by an in-house wide-bandgap PCM (Sb_2S_3) integration process. We show various non-volatile programmable devices, including micro-ring resonators, Mach-Zehnder interferometers and asymmetric directional couplers, with low loss (~0.0044 dB/μm), large phase shift (~0.012 π/μm) and high endurance (>5000 switching events with little performance degradation). Moreover, we showcase this platform's capability of handling relatively complex structures such as multiple PIN diode heaters in devices, each independently controlling an Sb_2S_3 segment. By reliably setting the Sb_2S_3 segments to fully amorphous or crystalline state, we achieved deterministic multilevel operation. An asymmetric directional coupler with two unequal-length Sb_2S_3 segments showed the capability of four-level switching, beyond cross-and-bar binary states. We further showed unbalanced Mach-Zehnder interferometers with equal-length and unequal-length Sb_2S_3 segments, exhibiting reversible switching and a maximum of 5 ($N+1, N=4$) and 8 ($2^N, N=3$) equally spaced operation levels, respectively. This work lays the foundation for future programmable very-large-scale PICs with deterministic programmability.

Programmable photonic integrated circuits (PICs)[1] can realize different functionalities by reconfiguring on-chip optical components and are at the heart of modern photonic technologies. They have enabled various applications, ranging from optical communication[2,3], light detection and ranging (LiDAR)[4–6], and optical interconnects[7] to classical[8–10] and quantum optical information processing[11,12]. There are four key requirements to scale such programmable PICs[1]—low static power consumption, compact component footprint, low insertion loss, and low crosstalk between different components. The reconfiguration speed, while critical for optical communications, is less important for many low-frequency applications in programmable

[1]Department of Electrical and Computer Engineering, University of Washington, Seattle, WA 98195, USA. [2]Department of Physics, University of Washington, Seattle, WA 98195, USA. [3]These authors contributed equally: Rui Chen, Virat Tara. ✉e-mail: charey@uw.edu; arka@uw.edu

PICs[13], such as inference in integrated optical neural networks[9,10,14], programmable microwave photonics[15], and multi-purpose photonic signal processing cores[16].

Non-volatile chalcogenide phase-change materials (PCMs)[13,17–19] stand out among many promising tuning mechanisms as they fulfill all key requirements for very-large-scale (VLS) programmable PICs. PCMs have two stable micro-structural phases with drastically different indices, under the ambient environment—amorphous (a-) and crystalline (c-) phases, leading to a unique non-volatile nature and a significant optical refractive index contrast ($\Delta n \sim O(1)$). As a result, they consume zero static power once switched and render a truly "set-and-forget" operation. The large index contrast Δn is also crucial to make ultra-compact integrated optical components, such as attenuators[20,21], phase shifters[22–24] and beam coupler[24–26] with length scale <100 μm. Prototypical PCMs such as GeSbTe (GST) are optimized in terms of phase-change speed for electronic memory applications, but they are not necessarily optimal for photonic applications due to the high absorption loss in the visible and near infrared (NIR) wavelength range[13]. Recently, emerging wide bandgap PCMs such as GeSbSeTe[27], Sb_2S_3[28] and Sb_2Se_3[29] offer negligible material absorption, showing promise for phase-only photonic applications. Moreover, amorphization of PCMs is immune to programming thermal crosstalk thanks to the threshold-driven nature[18] of the melt-quench process. As a result, any thermal crosstalk temperature below their melting point (usually >500 °C[29]) will not affect the on-chip components and the PIC works in a crosstalk-free fashion once the programming is finished. Although crystallization process is less thermal crosstalk immune due to its lower temperature thresholds (usually ~200 °C), such crosstalk can be handled by first crystallizing all the components and then amorphizing the desired ones[30].

Recent years has indeed witnessed significant advancements in PCM-based programmable PICs, controlled by short laser or electrical pulses for applications such as optical memories[31,32], programmable optical switches[20,21,23,24,33–36], low-power in-memory computing[10,14,37,38] and optical trimming[22,24]. Compared to the optical actuation scheme[10,14,31,33,39], the electrically controlled methods[20,21,23,24,26,35,36] eliminate the requirements for sophisticated and bulky pulsed laser setups. Therefore, they are more promising for a faster and more accessible real-time control, enabling true integration of the entire optical systems on a chip. Such accessibility is crucial for further expanding the usage of these PCM-based components/systems since electrical instruments such as voltage/current sources and function generators are much more affordable for the consumers than the sophisticated pulsed lasers. Surprisingly, the electrically controlled PCM-based PICs are still either in a single-device level[20–24,26,40], or a very small system scale[38]. This can primarily be attributed to the low yield of the in-house fabrication due to the more sophisticated fabrication steps compared to optical actuation schemes, such as multi-stage overlay lithography, doping, annealing, and growth of metal vias. This incurs a significantly prolonged designing and testing cycle. Moreover, inconsistencies in the in-house fabrication process causes difficulty in building a VLS PCM-based PIC system. While commercial foundries provide much more reliable silicon photonic components, PCMs are not directly available there yet.

In this work, we demonstrate a fast-prototyping approach to integrating a wide-bandgap PCM antimony trisulfide (Sb_2S_3) on wafer-scale silicon photonics. The pure silicon photonic wafers were fabricated in a 300 mm semiconductor fab. We then opened the oxide window on the silicon waveguides, and deposited Sb_2S_3 in-house. The PCM integration process is independent of the 300-mm fab process since it is at the back-end-of-line, therefore, no change is required on the 300 mm fab side. The process is also independent of the PCM used, providing a fast platform for PCM screening. To illustrate the versatility of this platform, we showed several different electrically controlled PCM-based silicon photonic devices operating in the telecommunication O-band (wavelength ~1330 nm), including micro-ring resonators (MRRs), Mach-Zehnder interferometers (MZIs), and asymmetric directional couplers (DCs), demonstrating low loss (~0.0044 dB/μm), large phase shift (~0.012 π/μm) and high endurance (>5000 switching events). To showcase the advantage of this fast-prototyping approach, we demonstrated a novel structure to realize deterministic multilevel operation in MZIs and asymmetric directional couplers using N interleaved PIN heaters to individually control each Sb_2S_3 segment to achieve a maximum of 2^N equally spaced operation levels by engineering the lengths of the Sb_2S_3 segments. This work demonstrates a promising approach to fast prototyping of PCMs for programmable PICs and shows a crucial step toward VLS programmable PICs by marrying the large-scale silicon photonics fab with in-house PCM integration process.

Results

Reproducible zero-change integration of PCMs on silicon photonics from a 300-mm fab

Figure 1a shows a schematic of the PCM-silicon hybrid photonics platform, on which different functional optical components are fabricated, including MRRs, MZIs and asymmetric DCs. All the components are armed with p++-intrinsic-n++ (PIN) doped silicon heaters for in situ electrical tuning of the PCMs. Electrical signals are applied on the platinum pads, which are well separated from the optical waveguides and are connected to the doped silicon regions by vertical metal vias. We emphasis that such multi-layer fabrication is crucial for low-loss routing of metal wires in VLS programmable PICs and is not available in our in-house fabrication. An in-house, easy-to-replicate fabrication process is developed to integrate Sb_2S_3 thin film on passive silicon waveguides (see Supplementary Fig. S1 and *Methods*). Compared to our previous fully in-house fabrication[24], this scheme shows five steps fewer electron-beam lithography (see discussion in Supplementary Section S1), significantly reducing the fabrication inconsistencies, manpower, and costs. The only critical in-house fabrication step is the Sb_2S_3 liftoff, which was optimized using a bilayer-PMMA to achieve uniform and consistent liftoff. Figure 1b shows the photograph of a 300 mm wafer fabricated by Intel, which is diced into 2.5 cm × 3.3 cm reticles. We developed an in-house process to open 4 μm-wide oxide windows followed by Sb_2S_3 deposition and patterning (see details in *Methods*). We performed optical mode simulations to quantify the scattering loss due to the oxide window, suggesting <−0.01 dB scattering loss (99.8% power coupling) per window. Such a small scattering loss comes from our 300 nm-thick waveguide, which confines 90.6% of optical mode in the silicon core. The in-house fabrication process can potentially be extended to whole-wafer level. An optical micrograph of the reticle after Sb_2S_3 integration is shown in Fig. 1c. We note that the excess optical loss arising from such in-house fabrication is negligible as optical mode perturbation caused by the oxide etching and Sb_2S_3 deposition is minor. This was verified by similar quality-factors (Q-factor) of the MRRs, which only slightly reduced from ~1.27×10^5 to ~1.01×10^5 (See Supplementary Fig. S2) after all the in-house fabrication processes. This implies an excess loss of only 0.02 dB for 20 μm-long Sb_2S_3. We highlight that such a highly scalable platform can immediately enable screening and fast testing of different PCMs by simply changing the sputtering targets or using other deposition methods such as evaporation. We also emphasize that the PCM integration process is at the back end of a 300-mm fab line, and zero change is required on the 300-mm fab process, crucial to reliable and massive production.

Reversible switching of the micro-ring resonators and Mach-Zehnder interferometers

We first demonstrate reversibly switchable MRRs and MZIs on this platform using electrical control. We will further show asymmetric DCs with deterministic multi-level behavior in the next section. Although the devices were designed and tested at telecom O-band (1260~1360 nm), we do not foresee any fundamental problem with extending the operation to the telecom C-band (~1550 nm) as Sb_2S_3 has even lower absorption loss in the longer wavelength regime (see Supplementary Fig. S3)[24,29,41]. Figure 2a shows an optical microscope image of a fabricated non-volatile tunable MRR loaded with 25 μm-long, 20 nm-thick Sb_2S_3 thin film. The PIN diode had a resistance of ~62.5 Ω and a turn-on voltage of ~0.8 V (see Supplementary Fig. S4). Figure 2b shows 5 reversible switching cycles with a resonance shift of ~0.40 nm by applying three electrical pulses with amplitude of 6.9 V

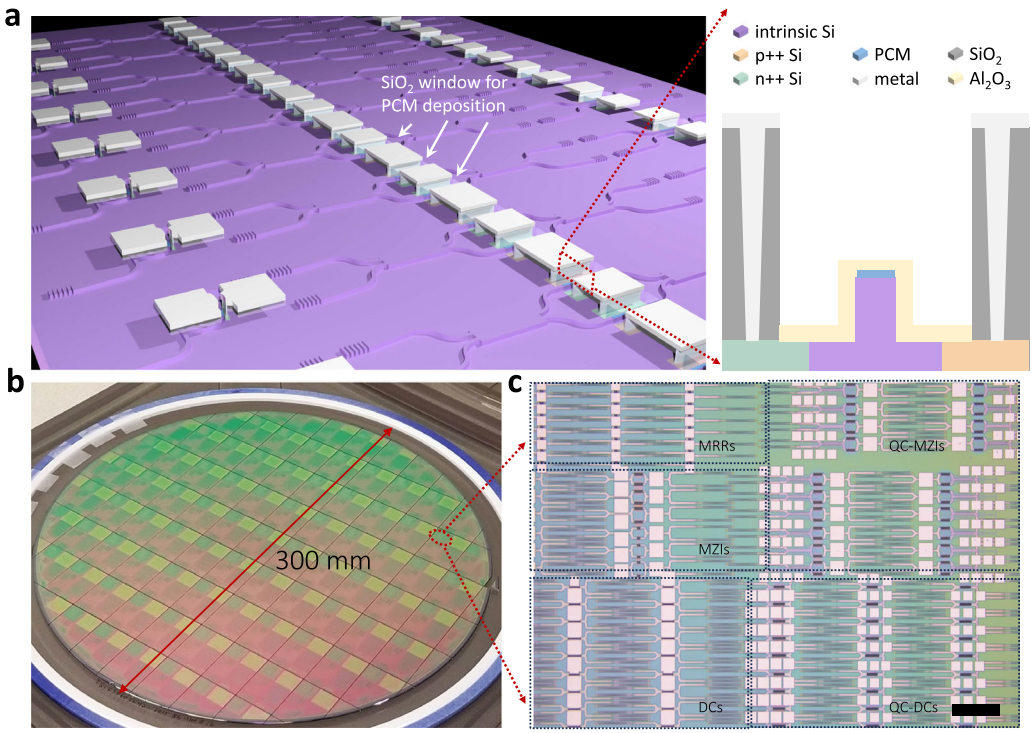

Fig. 1 | Schematic and photograph of the fabricated wafers and reticles. **a** Schematic of the silicon-PCM hybrid platform. The 300 mm semiconductor fab promises high-volume manufacturing, and many reticles can be fabricated simultaneously for fast prototyping. The PCMs are integrated in-house by opening an oxide window on the optical waveguides followed by deposition and patterning processes. A schematic showing the cross-sectional view of the PCM-silicon hybrid platform is on the right. **b** Photograph of the 300 mm pure silicon photonic wafer, which is diced into multiple 2.5 cm × 3.3 cm reticles. **c** Optical micrograph of a reticle after integrating the low-loss PCM Sb_2S_3, showing various optical components such as micro-ring resonators (MRRs), Mach-Zehnder interferometers (MZIs), asymmetric directional couplers (DCs), quasi-continuously (QC) tunable MZIs and DCs. (Scale bar: 500 μm) The zoomed-in optical micrographs of all components are in Figs. 2–4.

(2.9 V) and duration of 500 ns (200 ms) to switch the Sb_2S_3 into its a- (c-) phase. The free spectral range (FSR) of this MRR was measured as ~2.7 nm, suggesting a round-trip phase shift of ~0.3 π or 0.012 π/μm. This matches very well with the simulated phase shift ~0.0125 π/μm (see Supplementary Fig. S5), indicating a complete phase change of Sb_2S_3. By fitting the ring's spectrum to a Lorentzian line shape, we extracted a Q-factor of 5.66×10^4 (3.91×10^4) for a- (c-) Sb_2S_3. Therefore, the excess loss of c-Sb_2S_3 was estimated as 0.11 dB according to the Q-factor reduction[39], i.e., loss per π was around 0.4 dB, which is slightly higher than the simulated loss per π of ~0.26 dB (see Supplementary Fig. S5), and can be attributed to extra scattering at c-Sb_2S_3 grain boundaries[24]. We emphasize that the smaller resonance shift compared to recently reported results[24] is due to differences in the waveguide geometry as the waveguides here are thicker (300 nm compared to 220 nm) and narrower (400 nm compared to 500 nm), which significantly reduces the optical mode interaction with Sb_2S_3 (see Supplementary Fig. S6). To further increase the optical phase shift, we can design thinner and wider waveguides to enhance the light-matter interaction or use low-loss PCMs with a larger optical refractive index contrast such as Sb_2Se_3[22]. Another approach is to increase the PCM thickness, which, however, incurs additional optical scattering[22] and difficulty in reversible switching[42]. We note that the Q-factor reported here reduces compared to the initial Q-factor (~1.27×10^5) due to extra optical loss caused by carrier migration from the doping region to the intrinsic region after high voltage pulses were applied. This excess loss was estimated as ~0.2 dB and can be eliminated in the future by enlarging the intrinsic region width.

Similar to the MRR, low-loss phase shifter functionality was also demonstrated in an unbalanced MZI in Fig. 2c, where 60 μm-long, 20 nm-thick Sb_2S_3 was deposited on both arms. Figure 2d presents the reversible switching result of single arm for 5 cycles. Applying the amorphization (14.7 V, 500 ns) and crystallization (5.5 V, 200 ms) electrical pulses led to a resonance shift of ~0.75 nm for an FSR of ~6.3 nm, *i.e.*, a phase shift of ~0.24 π. The electrical voltage is higher than MRRs due to impedance mismatch with the function generator during measurement. Moreover, the longer metal wire also led to a lower unit length conductivity in this MZI (see Supplementary Fig. S4). We also note the MZI presents a smaller unit length phase shift (0.004 π/μm) than the MRR (0.012 π/μm). We attribute it to the relatively thick oxide residue on the MZI waveguides, which physically separated the optical modes from the Sb_2S_3 thin film and weakened the effective index contrast. This issue could be resolved by another wet-etch process to ensure complete removal of the oxide on waveguides.

Dual-arm controlled MZIs support push-and-pull type operation, as shown in Fig. 2e. With input light injected from the upper input port, switching the Sb_2S_3 to the c-phase on the upper (lower) arm led to a blue (red) spectral shift at the bar output port. We denote the structural phases σ of Sb_2S_3 on the upper and lower arms as a sequence $\sigma_u\sigma_l$. Figure 2eiii shows a large relative phase shift of ~0.7 π between *ca* and *ac* phase and four distinct levels. We attribute the difference in spectral shift on two arms to incomplete phase transition or material ablation, which can be improved by further optimizing the pulse conditions. Previous simulation suggested an ablation-free voltage range of 0.6~1.0 V, which highly depends on the PIN heater design[43]. For our PIN design and in experiment, we typically observed Sb_2S_3 ablation when the voltage was increased by 1~1.2 V (0.5~0.7 V) above the minimum amorphization (crystallization) voltage. The tighter crystallization parameter window is attributed to the much longer crystallization pulse duration (200 ms). We note that both the incomplete phase transition and the material ablation could be a result of non-uniform heating produced by sub-optimal heater design. If the center temperature is significantly higher than the surrounding temperature, the middle portion of PCMs may be amorphized (ablated) while materials at the edge remain unswitched[42]. In the future, a curved heater design[44] can be adopted to improve the heating uniformity hence a complete phase transition without material ablation. This MZI

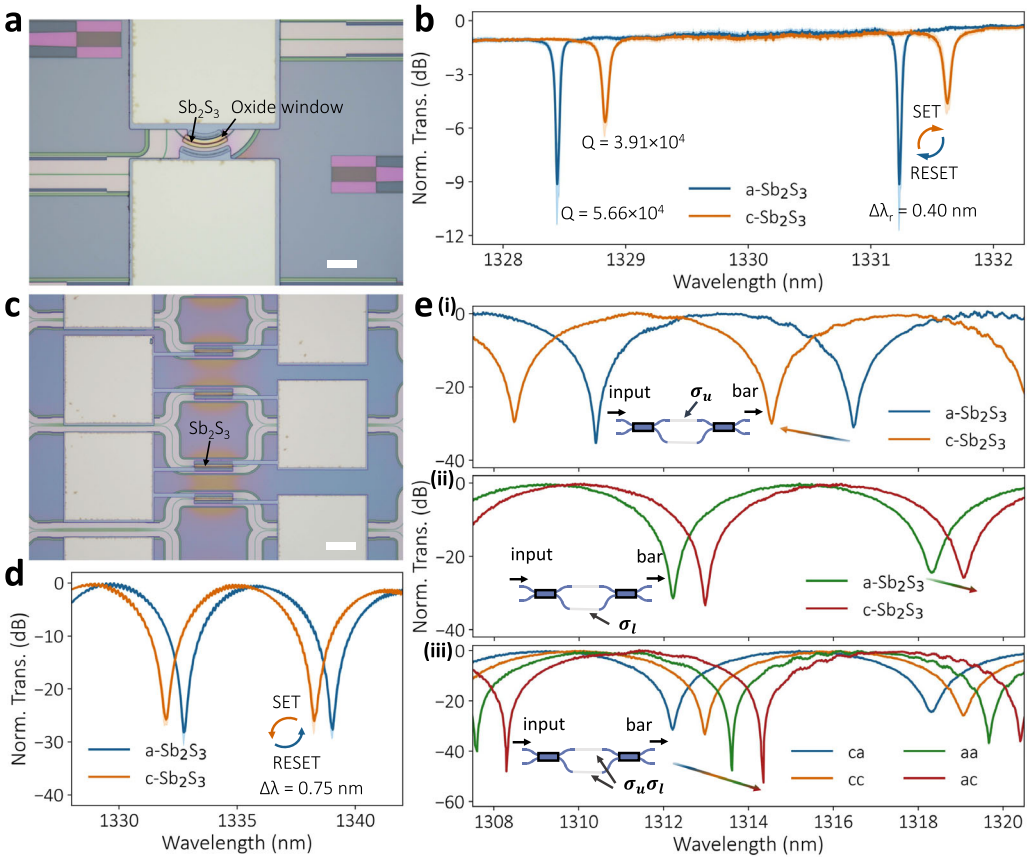

Fig. 2 | Reversible reconfiguration of micro-ring resonators and Mach-Zehnder interferometers through electrically controlled 20-nm-thick Sb_2S_3 thin films on silicon. a Optical micrograph image of an MRR. An MRR is coupled with waveguide, and only a small portion of the MRR is viewable due to the metal pads. (Scale bar: 20 μm) **b** Reversibly tuning an MRR for 5 cycles by electrically switching 20 nm-thick, 25 μm-long Sb_2S_3 thin film on the intrinsic waveguide. A resonance red shift $\Delta\lambda_r$ of 0.40 nm and Q-factor reduction from 5.66×10^4 to 3.91×10^4 were observed after Sb_2S_3 crystallization. The shaded region indicates the standard deviation. Pulse conditions: 6.9 V, 500 ns for amorphization and 2.9 V, 200 ms for crystallization. **c** Optical micrograph image of an MZI. (Scale bar: 50 μm) **d** Reversibly tuning of an unbalanced MZI for 5 cycles by electrically switching 20 nm-thick, 60 μm-long Sb_2S_3 thin film on the intrinsic waveguide. A spectral blue shift of 0.75 nm was observed. Pulse conditions: 14.7 V, 500 ns for amorphization and 5.5 V, 200 ms for crystallization. **e** Push-and-pull operation of the dual-arm reconfigurable MZI by independently controlling the upper and lower MZI arms, showcasing a larger phase shift and deterministic four-level operation. The structural phases of Sb_2S_3 on the upper σ_u and lower arm σ_l are denoted in the label as $\sigma_u\sigma_l$.

device maintained good optical contrast after more than 500 switching events (See Supplementary Fig. S7).

Deterministic quasi-continuous tuning in asymmetric directional couplers with two segments of independently controlled Sb_2S_3

On this scalable platform, we show a novel method to achieve deterministic multilevel or quasi-continuous tuning, which is generally a challenging task due to the inherent stochastic nature of electrically controlled PCMs[45]. Figure 3a shows our scheme, where multiple segments of Sb_2S_3 thin films are individually controlled using interleaved PIN doped silicon heaters. Each Sb_2S_3 segment is switched electrically and independently to fully-a- or fully-c-phase in a repeatable fashion. By encoding the state of each Sb_2S_3 segment, multiple deterministic operation levels were obtained. To avoid potential thermal crosstalk, the segments are separated by 1 μm. One potential pitfall of this scheme is the relatively complex structure, incurring a higher device failure rate due to fabricated dimension inconsistencies. In that regard, mature wafer-scale silicon photonic fab/foundries provide a reliable solution.

The design of the Sb_2S_3-loaded asymmetric DCs follows previous works[24,46]. Two waveguides of different widths are closely positioned to facilitate evanescent coupling, which allows optical power to transfer from one waveguide to the other. According to the coupled mode theory[47], the power transfer efficiency η is expressed by $\eta = \frac{1}{\sqrt{1+(\delta/\kappa_c)^2}}$, where $\delta = \frac{\pi}{\lambda_0}(n_2 - n_1)$ is the waveguide detuning, $\kappa_c = \frac{\pi}{\lambda_0}(n_e - n_o)$ is the coupling strength, $n_{1,2}$ is the effective refractive index for two waveguides assuming no coupling, $n_{e,o}$ is the effective index of the even (odd) super-modes formed by the coupled-waveguide system, λ_0 is the vacuum wavelength of light. The maximum power transfer efficiency $\eta_{\max} = 1$ is reached when $n_1 = n_2$, which is referred to as the phase-matching condition. In such phase-matched system, the coupling length L_c to achieve complete power transfer is expressed as $L_c = \frac{\pi}{2\kappa_c} = \frac{\lambda_0}{2(n_e - n_o)}$, where $n_{e,o}$ can be obtained from numerical simulators. In general, a larger gap between two waveguides leads to a smaller coupling strength κ_c and hence a longer L_c. To reconfigure the directional coupler, Sb_2S_3 is deposited and patterned on top of the narrower waveguide. The widths of the waveguides are carefully designed to achieve the phase matching condition in one state of Sb_2S_3, in our case, the a-state. When switching Sb_2S_3 it to the c-state, both the coupling strength κ_c and the waveguide detuning δ are changed due to effective index difference of the PCM loaded waveguide, thus a change in the output power. By judicious design of the gap, a complete switching from cross-state to bar-state can be achieved[46]. As such, selectively switching part of the Sb_2S_3 can provide intermediate output states[24,32,40]. It is important to highlight that while such intermediate levels naturally emerges with low-loss PCM Sb_2S_3, achieving them using absorptive PCMs like GST requires additional device design[13]. More detailed numerical simulation procedure and results can be found in Supplementary Figs. S8 and S9.

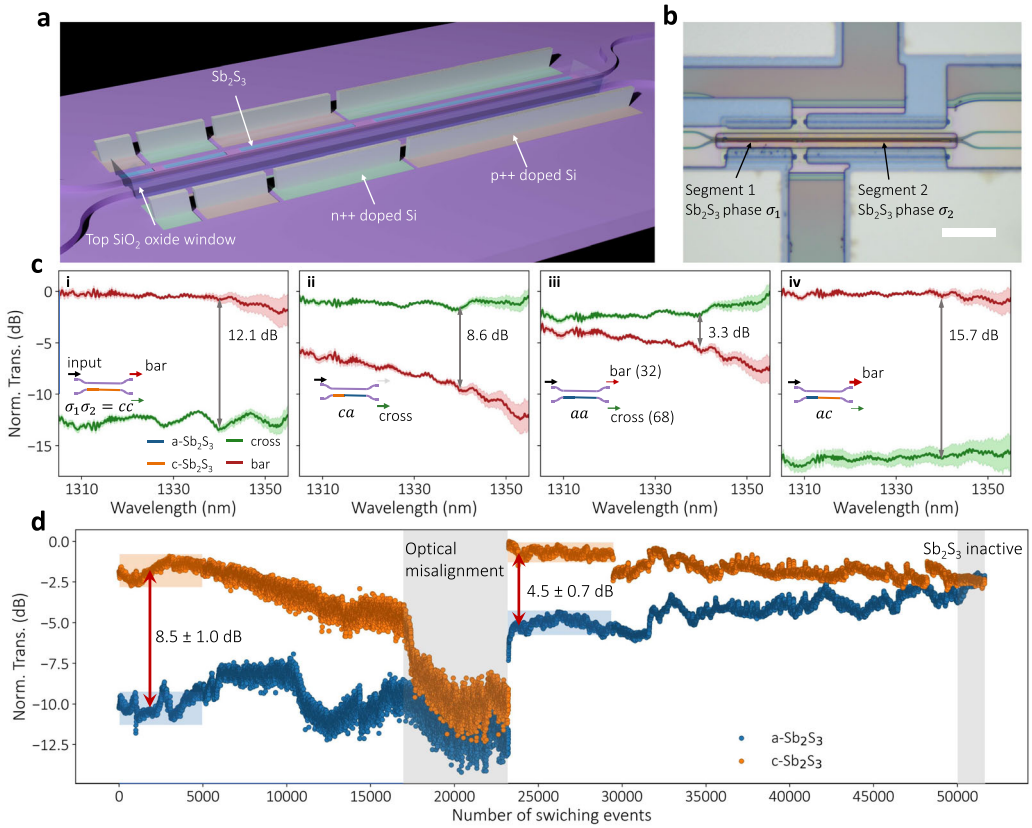

Fig. 3 | Quasi-continuously tunable asymmetric directional coupler with two individually controlled Sb_2S_3 segments. a Schematic with metal pads omitted for visualization, **b** Optical micrograph of an QC-DC with two Sb_2S_3 segments (Scale bar: 20 μm). **c** Transmission measurement results at both bar and cross port for different phase sequences of the material, demonstrating 4 operation levels: (i) cc (ii) ca (iii) aa (iv) ac, where we have denoted the phases of segments 1 and 2 as $\sigma_1\sigma_2$. The transmission spectra were normalized to a reference waveguide on chip. The device was reconfigured with electrical pulses five times and the shaded region indicates the standard deviation, showing excellent deterministic quasi-continuous tuning beyond binary levels. The switching condition was three 7.8 V, 500 ns pulses for amorphization and three 3 V, 200 ms pulses for crystallization. **d** Endurance test recording cross-port optical transmission while switching Sb_2S_3 Segment 2 at 1330 nm for 52,600 times (26,300 cycles). The switching condition was three 7.8 V, 500 ns pulses for amorphization and three 3.3 V, 2 ms pulses for crystallization. Little performance degradation was observed before 5000 switching events, exhibiting a large optical contrast of 8.5 ± 1.0 dB. The contrast decreases after then and an optical misalignment happens at around event 17,000, highlighted by the gray box labeled "optical misalignment". After realigning the setup, a contrast of 4.5 ± 0.7 dB was preserved. The Sb_2S_3 became inactive after around 50,000 switching events as indicated by the gray box labeled "Sb_2S_3 inactive".

As a proof-of-concept demonstration, we designed a two-segment asymmetric DC, which functions at bar(cross)-state when both Sb_2S_3 segments are in c(a)-phase, and other configurations function as intermediate levels (see Supplementary Fig. S9). Two segments were designed deliberately with different lengths to achieve four operation levels. Such multilevel asymmetric DC was fabricated, and Fig. 3b shows the microscope image, where the longer, 70 μm-long Sb_2S_3 segment (labeled 2) is twice as long as the shorter, 35 μm-long one (labeled 1). The orientation of the PIN diode heaters was designed to have opposite polarity to reduce unwanted crosstalk due to potential doping region mixing. The measured transmission spectra are shown in Fig. 3c, where the insets indicate the structural phase of each Sb_2S_3 segment. As shown in Fig. 3c(i), initially two Sb_2S_3 segments were in the cc-state, and the asymmetric DC guided the light to the bar-port with an insertion loss of ~0.7 dB and extinction ratio of ~12.1 dB at 1,343 nm. When switching Sb_2S_3 Segment 2 with short electrical pulses with amplitude of 7.8 V and duration of 500 ns, a complete spectrum flip was observed as in Fig. 3c(ii), exhibiting high cross-port transmission with an insertion loss of ~1.0 dB and an extinction ratio of ~8.6 dB at 1343 nm. We further amorphized Segment 1 using 7 Volt, 500 ns electrical pulses and measured spectra in Fig. 3ciii and c(iv). An intermediate operation level with a splitting ratio of ~32:68 between the bar- and cross-port was realized in Fig. 3c(iii). The extinction ratio increased from 12.1 dB in the cc-configuration to 15.7 dB in the ac-configuration. Segments 1 and 2 were switched back to c-phase with 3-Volt, 200-ms electrical pulses. We repeated the switching experiment 5 times and plot the standard deviation as the shaded region in Fig. 3c. The only slight standard deviation showcases the deterministic nature of this multi-segment approach. The discrepancy of the experimental performance from the simulation can be attributed to the fabrication imperfection and can be overcome by finer device parameter sweep during tape-out and better process control.

Figure 3d shows the cross-port transmission at 1,330 nm for 52,600 switching events by alternatively sending in amorphization and crystallization pulses to Segment 2. We note that one switching event is accomplished by applying three pulses, crucial for repeatable Sb_2S_3 phase transition[24]. To facilitate the cyclability test, we used three faster pulses for crystallization with amplitude 3.3 V and duration 2 ms and the amorphization pulses remained the same. The thermal stabilization time between pulses was set to ~40 ms, allowing us a rate of around $\frac{1}{3\times(40+2+0.5)ms} \approx 8Hz$ and to finish all 52,600 switching events within ~2 h. The optical contrast remained high ~8.5 ± 1.0 dB after 5,000 switching events, showcasing excellent cyclability. After that, we observed a gradual drift in the c-Sb_2S_3 level and a decrease in the contrast, which could be attributed to partial Sb_2S_3 damage. The latter may also be a result of PIN heater degradation indicated by the IV characteristics change after 52,600 events (see Supplementary Fig. S10). As such, we had to increase the amorphization (crystallization) pulse amplitude to 8.3 V (3.3 V) at event 17,000. An optical misalignment occurred at ~17,000 switching events, indicated by a low optical transmission level and is highlighted in Fig. 3d by a gray box region. After we

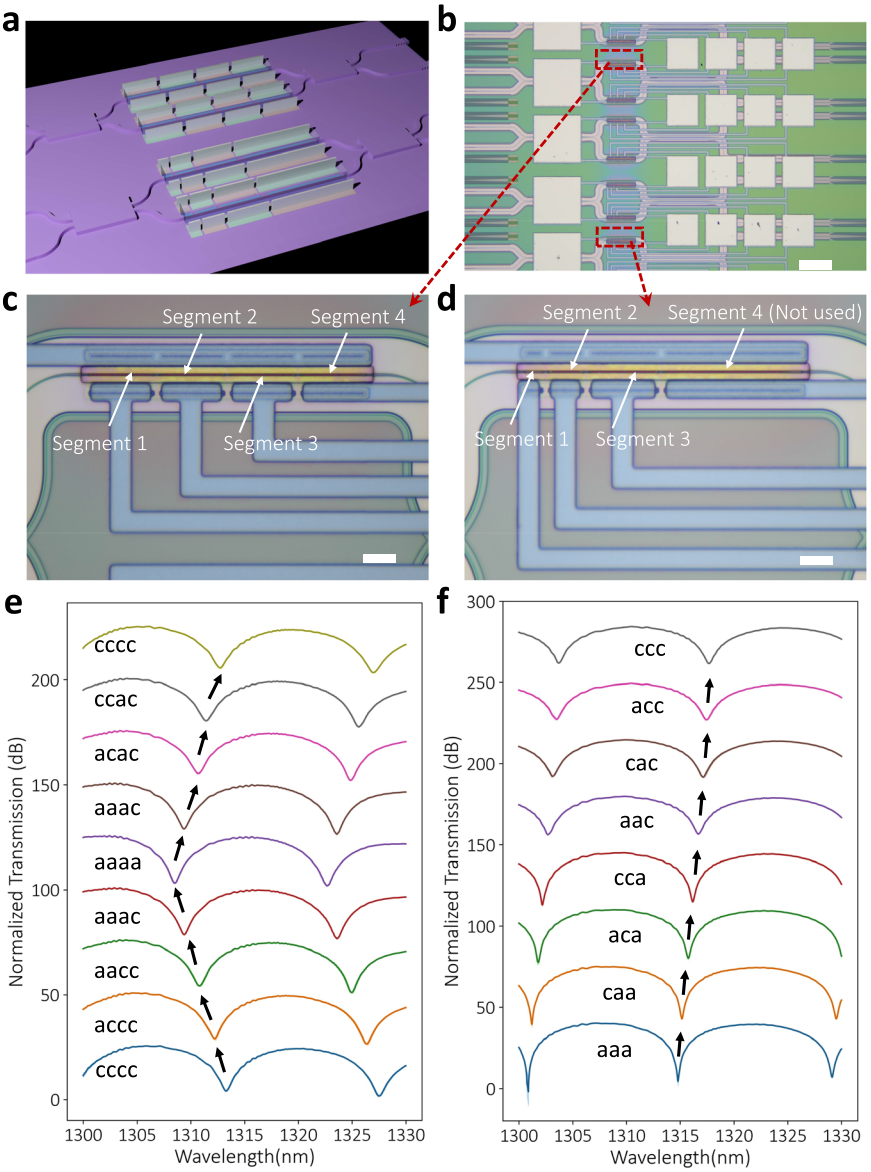

Fig. 4 | Quasi-continuously tunable Mach-Zehnder interferometers with four equal and unequal Sb_2S_3 segments. a Schematic, **b** Optical micrograph of the quasi-continuously tunable MZIs with equal and unequal Sb_2S_3 segments. (Scale bar: 100 μm) **c**, **d** Zoomed-in optical micrograph of (**c**) equal (**d**) unequal Sb_2S_3 segment lengths. (Scale bar: 10 μm) **e** Measured optical transmission spectra after gradual amorphization of equal-length Sb_2S_3 segments. Five operation levels were achieved with spectral shift of 1.125 ± 0.26 nm per step. Reversible switching was demonstrated by bringing the system level back through one-by-one crystallization in a different order. The structural phase of Sb_2S_3 segments is indicated near each curve with the same convention in Fig. 3. **f** Experimental demonstration of 8 ($2^N, N = 3$) operation levels enabled by unequal segment lengths in a geometric series with common ratio of 2. The spectrum is continuously shifted with uniform step resonance shift of 0.41 ± 0.12 nm or 0.059π. We highlight that measurement for both (**e**) and (**f**) were repeated five times and the shaded regions indicate the standard deviation. The barely visible shaded region indicates a highly deterministic quasi-continuous operation. (Note: metal pads were omitted in the schematic for visualization).

realigned the optical setup and increased the pulse amplitude, the optical contrast recovered to ~4.5 ± 0.7 dB until approximate event 30,000, and gradually decreased again. The Sb_2S_3 stopped responding to any electrical pulses after 50,000 switching events. Scanning electron microscope images (see Supplementary Fig. S11) shows some black areas at the edge of waveguides after the cyclability test, which could be a result of Sb_2S_3 ablation or thermal reflowing. Several strategies can be used to further improve the cyclability, such as developing more endurable PCMs[35], engineering the thickness and material of the encapsulation layer[48], patterning the PCMs into subwavelength nanostructures[49], and engineering the microheaters and pulse conditions to provide a uniform temperature distribution[44].

Quasi-continuous tunable MZIs with equal and unequal-length multi-segments schemes

The quasi-continuous tuning idea was further extended to more Sb_2S_3 segments for a larger number of operation levels in unbalanced MZIs under single-arm operation in Fig. 4a. We designed, fabricated, and characterized two types of devices, with N Sb_2S_3 segments having the same or different lengths. Since the phase shift $\Delta\varphi$ induced by each Sb_2S_3 segment is proportional to its length, the equal length scheme loses some encoding capability by the redundant Sb_2S_3 configurations, leading to $(N + 1)$ level. In the unequal-length scheme, we design the lengths of segments as a geometric sequence with a common ratio of 2. For example, we denote the length of Sb_2S_3 segment i as L_i, then $L_1 : L_2 : L_3 = 1 : 2 : 4$ for a three-segment device. Redundancies in this configuration were avoided, and the system implemented at most 8 ($2^N, N = 3$) distinct levels with equal channel spacing.

Figure 4b shows the optical microscope image of the fabricated quasi-continuously tunable MZIs with four equal (see zoomed-in picture in Fig. 4c) and unequal (see zoomed-in picture in Fig. 4d) Sb_2S_3 segments. In both cases, the total length of four Sb_2S_3 segments was ~80 μm to provide a large phase shift. Figure 4e shows the measured results for the equal length scheme, where we achieved 5 ($N + 1, N = 4$) operation levels and demonstrated reversible switching between different levels. We first tested the pulse conditions of each segment with measured impedance of ~106, 130, 156, 185 Ω. This variation could be attributed to the difference in the metal wires' length and could be resolved by engineering the geometry of these wires. However, we note the switching voltage levels were similar after matching the load impedance of the function generator, showing less than ±0.5 V variation for amorphization. We used three ~8.8 V, 500 ns (~3.6 V, 200 ms) pulses for amorphization (crystallization). The waterfall plot of Fig. 4e shows the measured bar-port spectrum labeled with Sb_2S_3 segments'

phases when light was injected from the upper input port and tuning the lower MZI arm. All Sb_2S_3 segments were first set to the c-state, then amorphized one-by-one from Segment 1 to Segment 4. A gradual blue shift is observed, agreed with the smaller refractive index of a-Sb_2S_3 compared to c-Sb_2S_3. The Sb_2S_3 segments were then crystallized one-by-one in a different order until all were switched to the c-phase. Figure 4e shows that the final transmission spectrum (the top curve) aligning well with the initial one (the bottom curve), indicating a reversible switching behavior. The spectral shift was estimated as 1.125 ± 0.26 nm per step. The slight non-uniformity of the spectral shift could be attributed to incomplete phase change in the Sb_2S_3 segments and non-uniformity of Sb_2S_3 films, which could be resolved by further optimizing the electrical pulse condition and the fabrication process. We emphasize that no thermal crosstalk was observed, showcasing the thermal-crosstalk-free advantage of PCM tuning.

Compared to the equal length scheme, which only achieves $N + 1$ distinct optical levels, the unequal length scheme can achieve a maximum of 2^N levels with N Sb_2S_3 segments due to the strictly non-redundant configurations. Figure 4f shows our measurement results with three unequal Sb_2S_3 segments with a total length of 40 μm. The longest Segment 4 was not used in this proof-of-concept experiment. Like the previous experiment for the equal length scheme, we first set all the Sb_2S_3 segments to the a-phase, and then programmed the binary phases of three Sb_2S_3 segments to demonstrate 3 bits or 8 ($2^N, N = 3$) distinct levels by different combination of the segments' phases, labeled in Fig. 2f. We report a uniform step resonance shift of ~0.41 ± 0.12 nm and a step phase shift of ~0.059 π. We note that we observed a red shift when amorphizing the upper arm in another MZI and achieved a larger spectral shift after pulse condition optimization (see Supplementary Fig. S12 and explanation in Section S11). Such an exponential increase in the number of levels is critical to reduce the complexity of the control circuits for large-scale integration. We emphasize that the measurements for both equal-length and unequal-length devices were repeated for five reversible switching cycles. The standard variation was shown by a barely visible shaded region in Fig. 4e, f, implying a highly deterministic quasi-continuous tuning behavior.

Discussion

We note that this idea of using multiple segments of PCMs has been shown recently in another work with a different PCM GSSe and tungsten heaters[32]. However, it was limited to pure-amplitude modulation in a 1 × 1 waveguide switch. Here we show phase-only modulation with the low-loss PCM Sb_2S_3 in 2 × 2 asymmetric directional couplers and MZIs, which are crucial building blocks for large-scale PICs. We note although we only demonstrated integrating Sb_2S_3, any other PCMs can be easily tested on this versatile platform by simply changing the sputtering targets or using different deposition methods such as evaporation. Such a platform can open new opportunities in fast-prototyping and examination of PCMs. Lastly, we compare our scalable platform with other existing PCM-PIC works in Supplementary Table 1, showing similar performance. The energy efficiency for switching can be further improved by reducing the distance from the waveguides to metal vias to reduce series resistance of the PIN diodes.

In summary, we demonstrated a scalable programmable PIC platform by combining the mature and reliable 300 mm silicon photonic fab with in-house backend-of-line integration of the low-loss PCM Sb_2S_3. Non-volatile electrically programmable MRRs, MZIs, and asymmetric directional couplers were shown with low loss, large phase shift, and high endurance. Moreover, thanks to the platform's capability of handling complex structures, we showed a novel scheme to achieve deterministic multi-level operation by independently controlling multiple Sb_2S_3 segments. We experimentally demonstrated such deterministic quasi-continuous tuning behavior in both asymmetric directional couplers and MZIs, showcasing at most N bits or 2^N optical levels with N Sb_2S_3 segments by careful geometry engineering. Overall, our work lays the foundation for very-large-scale programmable PICs with zero-static power consumption and deterministic multi-level operations.

Methods

Optical design

We used Ansys Lumerical finite-difference eigenmode (FDE) simulator to simulate the Sb_2S_3-based phase shifter and design the asymmetric DC, for which a Lumerical script was developed and can be found online at https://github.com/charey6/Lumerical-Mode-PCM-DCs.git. The Ansys Lumerical finite-difference time-domain (FDTD) simulator was used to verify the optical performance of the quasi-continuously tunable asymmetric DC designed by FDE.

In-house fabrication process to integrate PCMs onto reticles by 300 mm silicon photonic fab

The initial pure silicon photonic chips were fabricated in a 300 mm semiconductor fab in Intel Corp., with silicon etch, doping, top oxide layer growth and metal vias growth included. We note that metallization was not available from the commercial manufacturing process at the time of tape-out, but it is now possible with a thicker SiO_2 top cladding layer. We can include the metallization in the future once we develop and test the window opening process for thicker SiO_2 cladding. The 300-mm wafer was then diced to 2.5 cm × 3.3 cm reticles for in-house Sb_2S_3 integration. The oxide window for Sb_2S_3 deposition on the intrinsic silicon waveguide was defined by an overlay using a direct write laser lithography tool (DWL, Heidelberg DWL66+) with adhesion-promoting primer HMDS (Yeild Engineering Systems, LP 3 A) and a positive tone resist AZ-1512 (~1 μm), followed by a partial dry etch of ~600 nm SiO_2 in a fluorine-based inductively coupled plasma etcher (ICP, Oxford PlasmaLab 100 ICP-18). The reticle was then immersed in 10:1 buffered oxide etcher (BOE) for 3 ~ 4 min for complete SiO_2 removal. To form an ideal Ohmic contact, removal of the surface oxide (~100 nm) on the metal vias was done by a second DWL overlay and immersing the chips in 10:1 BOE for 75 s. The metal contacts were then immediately patterned by a third DWL overlay using a negative tone resist NR9G-3000PY. Metallization of Ti/Pt (15 nm/200 nm) was done by electron-beam evaporation (CHA SEC-600) and lift-off. The Sb_2S_3 window was defined by JEOLJBX-6300FS 100 kV electron-beam lithography (EBL) using positive-tone resist double layer P(MMA-MAA) Copolymer and PMMA for high-quality liftoff process. A layer of 40 nm-thick Sb_2S_3 thin film was deposited using an 3-inch Sb_2S_3 target (Plasmaterial Ltd.) in a magnetron sputtering system (Lesker Lab 18) in Argon environment with sputtering power of 27 W and pressure of 3.5 mTorr, followed by a lift-off process. We note the actual Sb_2S_3 thickness after the liftoff was reduced to ~20 nm due to the trench effect, that the narrow resist trench lowered the deposition rate. This effect was verified by atomic force microscopy measurements[24]. We then encapsulated the Sb_2S_3 with 40 nm-thick Al_2O_3 through thermal ALD (Oxford Plasmalab 80PLUS OpAL ALD) at 150 °C. We emphasize that the relatively thick, high-quality Al_2O_3 capping along with the thin Sb_2S_3 film is crucial to reduce PCM thermal reflowing or redistribution after many cycles, and hence a consistent optical performance. To ensure good contact between the electric probe and metal pads while applying electrical pulses, the Al_2O_3 on the metal contacts was removed by defining a window using a fourth DWL overlay with positive tone resist AZ1512, then etching in a chlorine-based inductively coupled plasma etcher (ICP-RIE, Oxford PlasmaLab 100 ICP-18).

Optical transmission measurement setup

The silicon-Sb_2S_3 hybrid devices were measured in a 20°-angled vertical fiber-coupling setup. The stage temperature was kept constant at 26 °C by a thermoelectric controller (TEC, TE Technology TC-720) to ensure no thermal drifts in temperature-sensitive devices during the measurement, such as micro-ring resonators. We note that the TEC does not have any impact on the reversible phase transition of Sb_2S_3 since its phase transition temperature is much higher, i.e. ~300 °C (550 °C) for crystallization (amorphization). A tunable continuous-wave laser (Santec TSL-510) sent the input laser light, the polarization of which was controlled by a manual fiber polarization controller (Thorlabs FPC526) to achieve a maximum fiber-to-chip coupling efficiency. A low-noise power meter (Keysight

81634B) measured the static optical transmission. For the on-chip electrical switching, electrical pulses were applied to the on-chip metal contacts via a pair of electrical probes on two probe positioners (Cascade Microtech DPP105-M-AI-S). The crystallization and amorphization pulses were generated from a pulse function arbitrary generator (Keysight 81160 A). The tunable laser, power meter, thermal controller, source meter, and pulse function arbitrary generator were controlled by a LabView program. We emphasize that the speed of our cyclability measurement is limited to ~40 ms for each pulse by the LabView program, which takes a long time to communicate with and reconfigure the pulse generator. In the future, a continuous and repeating wavefront may be programmed in the pulse generator to allow faster endurance characterization.

Data availability

The data that support the findings of this study are available from the corresponding author upon request.

Received: 8 December 2023; Accepted: 28 February 2024;
Published online: 03 June 2024

References

1. Bogaerts, W. et al. Programmable photonic circuits. *Nature* **586**, 207–216 (2020).
2. Xu, Q., Schmidt, B., Pradhan, S. & Lipson, M. Micrometre-scale silicon electro-optic modulator. *Nature* **435**, 325–327 (2005).
3. Sharma, J. et al. Silicon photonic microring-based 4 × 112 Gb/s WDM transmitter with photocurrent-based thermal control in 28-nm CMOS. *IEEE JSSC.* **57**, 1187–1198 (2022).
4. Zhang, X., Kwon, K., Henriksson, J., Luo, J. & Wu, M. C. A large-scale microelectromechanical-systems-based silicon photonics LiDAR. *Nature* **603**, 253–258 (2022).
5. Poulton, C. V. et al. Coherent LiDAR with an 8,192-element optical phased array and driving laser. *IEEE J. Sel. Top. Quantum Electronics* **28**, 1–8 (2022).
6. Li, B., Lin, Q. & Li, M. Frequency–angular resolving LiDAR using chip-scale acousto-optic beam steering. *Nature* **620**, 316–322 (2023).
7. Cheng, Q., Bahadori, M., Glick, M., Rumley, S. & Bergman, K. Recent advances in optical technologies for data centers: a review. *Optica, OPTICA* **5**, 1354–1370 (2018).
8. Shen, Y. et al. Deep learning with coherent nanophotonic circuits. *Nat. Photonics* **11**, 441–446 (2017).
9. Xu, X. et al. 11 TOPS photonic convolutional accelerator for optical neural networks. *Nature* **589**, 44–51 (2021).
10. Feldmann, J. et al. Parallel convolution processing using an integrated photonic tensor core. *Nature* **589**, 52–58 (2021).
11. Harris, N. C. et al. Quantum transport simulations in a programmable nanophotonic processor. *Nat. Photonics* **11**, 447–452 (2017).
12. Saxena, A., Manna, A., Trivedi, R. & Majumdar, A. Realizing tight-binding Hamiltonians using site-controlled coupled cavity arrays. *Nat. Commun.* **14**, 5260 (2023).
13. Chen, R. et al. Opportunities and challenges for large-scale phase-change material integrated electro-photonics. *ACS Photonics* **9**, 3181–3195 (2022).
14. Wu, C. et al. Programmable phase-change metasurfaces on waveguides for multimode photonic convolutional neural network. *Nat. Commun.* **12**, 96 (2021).
15. Zhuang, L., Roeloffzen, C. G. H., Hoekman, M., Boller, K.-J. & Lowery, A. J. Programmable photonic signal processor chip for radiofrequency applications. *Optica* **2**, 854 (2015).
16. Pérez, D. et al. Multipurpose silicon photonics signal processor core. *Nat. Commun.* **8**, 1–9 (2017).
17. Youngblood, N., Ríos Ocampo, C. A., Pernice, W. H. P. & Bhaskaran, H. Integrated optical memristors. *Nat. Photon.* **17**, 561–572 (2023).
18. Fang, Z., Chen, R., Zheng, J. & Majumdar, A. Non-volatile reconfigurable silicon photonics based on phase-change materials. *IEEE J. Sel. Top. Quantum Electron.* **28**, 8200317 (2022).
19. Zhang, Y. et al. Myths and truths about optical phase change materials: a perspective. *Appl. Phy. Lett.* **118**, 210501 (2021).
20. Zheng, J. et al. Nonvolatile electrically reconfigurable integrated photonic switch enabled by a silicon PIN diode heater. *Adv. Mater.* **32**, 2001218 (2020).
21. Zhang, H. et al. Nonvolatile waveguide transmission tuning with electrically-driven ultra-small GST phase-change material. *Sci. Bull.* **64**, 782–789 (2019).
22. Ríos, C. et al. Ultra-compact nonvolatile phase shifter based on electrically reprogrammable transparent phase change materials. *PhotoniX* **3**, 26 (2022).
23. Fang, Z. et al. Ultra-low-energy programmable non-volatile silicon photonics based on phase-change materials with graphene heaters. *Nat. Nanotechnol.* **17**, 842–848 (2022).
24. Chen, R. et al. Non-volatile electrically programmable integrated photonics with a 5-bit operation. *Nat Commun* **14**, 3465 (2023).
25. Xu, P., Zheng, J., Doylend, J. K. & Majumdar, A. Low-loss and broadband nonvolatile phase-change directional coupler switches. *ACS Photonics* **6**, 553–557 (2019).
26. Chen, R. et al. Broadband nonvolatile electrically controlled programmable units in silicon photonics. *ACS Photonics* **9**, 2142–2150 (2022).
27. Zhang, Y. et al. Broadband transparent optical phase change materials for high-performance nonvolatile photonics. *Nat. Commun.* **10**, 4279 (2019).
28. Dong, W. et al. Wide bandgap phase change material tuned visible photonics. *Adv. Funct. Mater.* **29**, 1806181 (2019).
29. Delaney, M., Zeimpekis, I., Lawson, D., Hewak, D. W. & Muskens, O. L. A new family of ultralow loss reversible phase-change materials for photonic integrated circuits: Sb2S3 and Sb2Se3. *Adv. Funct. Mater.* **30**, 2002447 (2020).
30. Fang, Z. et al. Non-volatile phase-only transmissive spatial light modulators. *arXiv* https://doi.org/10.48550/arXiv.2307.12103 (2023).
31. Rios, C. et al. Integrated all-photonic non-volatile multi-level memory. *Nature Photonics* **9**, 725–732 (2015).
32. Meng, J. et al. Electrical programmable multilevel nonvolatile photonic random-access memory. *Light Sci Appl* **12**, 189 (2023).
33. Delaney, M. et al. Non-volatile programmable silicon photonics using an ultralow loss Sb2Se3 phase change material. *Science Advances* **7**, eabg3500 (2021).
34. Fang, Z. et al. Arbitrary programming of racetrack resonators using low-loss phase-change material Sb2Se3. *Nano Lett* **24**, 97–103 (2023).
35. Xia, J. et al. Ultrahigh endurance and extinction ratio in programmable silicon photonics based on a phase change material with ITO heater. *Laser Photonics Rev*. https://doi.org/10.1002/lpor.202300722 (2024).
36. Xia, J. et al. Seven bit nonvolatile electrically programmable photonics based on phase-change materials for image recognition. *ACS Photonics* **11**, 723–730 (2024).
37. Ríos, C. et al. In-memory computing on a photonic platform. *Sci. Adv.* **5**, 1–10 (2018).
38. Zhou, W. et al. In-memory photonic dot-product engine with electrically programmable weight banks. *Nat. Commun.* **14**, 2887 (2023).
39. Zheng, J. et al. GST-on-silicon hybrid nanophotonic integrated circuits: a non-volatile quasi-continuously reprogrammable platform. *Opt. Mater. Express* **8**, 1551 (2018).
40. Zhang, C. et al. Nonvolatile multilevel switching of silicon photonic devices with In2O3/GST segmented structures. *Adv. Opt. Mater.* **11**, 2202748 (2023).
41. Fang, Z. et al. Non-volatile reconfigurable integrated photonics enabled by broadband low-loss phase change material. *Adv. Opt. Mater.* **9**, 2002049 (2021).

42. Prabhathan, P. et al. Roadmap for phase change materials in photonics and beyond. *iScience* **26**, 107946 (2023).
43. Erickson, J. R., Shah, V., Wan, Q., Youngblood, N. & Xiong, F. Designing fast and efficient electrically driven phase change photonics using foundry compatible waveguide-integrated microheaters. *Opt. Express* **30**, 13673 (2022).
44. Zhang, Y. et al. Electrically reconfigurable non-volatile metasurface using low-loss optical phase-change material. *Nat. Nanotechnol.* **16**, 661–666 (2021).
45. Tuma, T., Pantazi, A., Le Gallo, M., Sebastian, A. & Eleftheriou, E. Stochastic phase-change neurons. *Nature Nanotechnology* **11**, 693–699 (2016).
46. Teo, T. Y. et al. Comparison and analysis of phase change materials-based reconfigurable silicon photonic directional couplers. *Opt. Mater. Express, OME* **12**, 606–621 (2022).
47. Osgood, R. & Meng, X. *Principles of Photonic Integrated Circuits: Materials, Device Physics, Guided Wave Design* (Springer Nature, 2021).
48. Martin-Monier, L. et al. Endurance of chalcogenide optical phase change materials: a review. *Opt. Mater. Express* **12**, 2145–2167 (2022).
49. Wu, C. et al. Low-loss integrated photonic switch using subwavelength patterned phase change material. *ACS Photonics* **6**, 87–92 (2019).

Acknowledgements

The authors would like to acknowledge Intel Corp. for fabrication of the silicon photonics wafers and thank John Heck, Harel Frish, Haisheng Rong for useful discussions. The research is funded by National Science Foundation (NSF-1640986, NSF-2003509), ONR-YIP Award, DARPA-YFA Award, and Intel. Part of this work was conducted at the Washington Nanofabrication Facility/ Molecular Analysis Facility, a National Nanotechnology Coordinated Infrastructure (NNCI) site at the University of Washington, with partial support from the National Science Foundation via awards NNCI-1542101 and NNCI-2025489. Part of this work was performed at the Stanford Nano Shared Facilities (SNSF), supported by the National Science Foundation under award (ECCS-1542152).

Author contributions

R.C. and A.M. conceived the project. R.C. designed the reconfigurable hybrid Sb_2S_3-silicon devices, ran the 300-mm silicon photonic tape-out, performed the in-house integration of Sb_2S_3 thin films to the silicon photonic devices, performed optical characterizations and data analysis. V.T. developed and performed the in-house integration process of Sb_2S_3, characterized the devices and helped with data analysis. M.C. helped with the in-house fabrication. M.C., J.D., J.S. and J.Y. helped with the characterization and data analysis. J.Z. and Z.F. helped with the design of the devices. A.M. supervised and planned the project. R.C. wrote the manuscript with input from all the authors.

Competing interests

The authors declare no competing interests.

Additional information

Supplementary information The online version contains supplementary material available at https://doi.org/10.1038/s44310-024-00009-6.

Correspondence and requests for materials should be addressed to Rui Chen or Arka Majumdar.